Journal of Computational Acoustics, Vol. 21, No. 1 (2013) 1250017 (29 pages)

DOI: 10.1142/S0218396X12500178

INTERNATIONAL ASSOCIATION
FOR MATHEMATICS AND
COMPUTERS IN SIMULATION

SIMULATION OF A MIXTURE MODEL FOR ULTRASOUND PROPAGATION THROUGH CANCELLOUS BONE USING STAGGERED-GRID FINITE DIFFERENCES

ROBERT P. GILBERT*, PHILIPPE GUYENNE† and JING LI‡
Department of Mathematical Sciences
University of Delaware, Newark, DE 19716, USA
*gilbert@math.udel.edu
†guyenne@math.udel.edu
‡jli@math.udel.edu

Received 6 December 2011
Accepted 8 May 2012
Published 9 November 2012

In this paper we treat the cancellous bone as is done in mixture theory, i.e. each point in the material has both a fluid and a solid phase co-existing there. Each phase is weighted by the volume fraction of material in the composite structure. It is seen that in such a material attenuation of amplitude as frequency increases occurs as is observed in laboratory experiments[33,34] and as was observed in the finite element homogenization approach used by Hackl, Ilic and Gilbert.

Keywords: Ultrasound; cancellous bone; staggered grid method.

1. Introduction

Osteoporosis is characterized by a decrease in strength of the bone matrix. Currently, bone mineral density (BMD) is the gold standard for *in vivo* assessment of fracture risk of bones and is measured using X-ray absorptiometric techniques.[11] However, only 70%–80% of the variance of bone strength is accounted for by bone density. As the brittleness of bone depends on more factors than bone density, biologists believe that quantitative ultrasound techniques could provide an important new diagnostic tool.[14,18,49] Moreover, in contrast to X-ray densitometry, ultrasound does not ionize the tissue, and its implementation is relatively inexpensive. Since the loss of bone density and the destruction of the bone microstructure is most evident in osteoporosis cancellous bone, it is natural to consider the possibility of developing accurate ultrasound models for the isonification of cancellous bone. Ultrasound has been considered as a means to characterize the elastic properties of cortical and cancellous bone for some time.[2–4,6–9,12–14,16,17,24,28,30,35,36,38,40,48,49,52–55,57,60,63–66] One particular ultrasonic technique for assessing BMD is by calcaneal broadband ultrasonic attenuation (BUA) and speed of sound which are highly correlated with calcaneal BMD.[21,63] In this method, the time is measured for sound to travel, in water, the distance between the two transducers. Then the experiment is repeated with a bone sample placed between the two transducers. Two time measurements are taken, first without the bone sample in place and then with the bone sample in place. From the velocity of sound in water, and the size of the bone sample, the velocity of the compression wave through the bone sample can be calculated.

In Ref. 5 three-dimensional numerical simulations of ultrasound transmission were performed. Synchrotron microtomography provided high resolution three-dimensional images of bone structures, which were used as the input geometry. It was found that simulations reproduced phenomena observed in experiments, such as the speed of sound, and the slope of the normalized frequency-dependent attenuation.

2. The Composite Model

Cancellous bone may be thought of as consisting of a solid matrix with an interstitial fluid. In the case of defatted bone, the acoustic interrogation is accomplished *in vitro* as mentioned in Sec. 1. In the *in vivo* case, the interstitial fluid is a blood–marrow mixture. Our idea is to use a mixture theory approach which assumes that, at any position in the cancellous bone, there are both a solid phase (trabeculae) and a fluid phase (water or blood–marrow). We accomplish this by including both the solid and the fluid as part of a general system. In this way, the stress tensor of the composite material is given by

$$\tau = \Theta\tau^f + (1-\Theta)\tau^s, \tag{1}$$

where Θ is the characteristic function of the fluid phase, i.e. $\Theta = 1$ in the fluid region (denoted by the superscript f), while $\Theta = 0$ in the solid region (denoted by the superscript s).

The solid constitutive equations may be written in the generalized form

$$\tau^s_{ij} = A^s_{ijkl} e(\mathbf{u})_{kl} + B^s_{ijkl} e(\mathbf{v})_{kl}, \tag{2}$$

where the A^s_{ijkl} are the elasticity coefficients of the solid and are assumed to have the classical symmetry and positivity properties, i.e.

$$A^s_{ijkl} e_{ij} e_{kl} \geq 0, \quad A^s_{ijkl} = A^s_{klij} = A^s_{jikl} = A^s_{ijlk},$$

while the B^s_{ijkl} correspond to instantaneous viscosity terms. The strain tensors are defined by

$$e(\mathbf{u})_{ij} := \frac{1}{2}(\partial_j u_i + \partial_i u_j), \quad e(\mathbf{v})_{ij} := \frac{1}{2}(\partial_j v_i + \partial_i v_j), \tag{3}$$

where $\mathbf{u}$ and $\mathbf{v}$ denote the displacement and velocity vector fields, respectively. The notation ∂_j is shorthand for partial differentiation with respect to the subscript j. In the isotropic elastic case, the A^s_{ijkl} become

$$A^s_{ijkl} e_{kl} = (\lambda\delta_{ij}\delta_{kl} + 2\mu\delta_{ik}\delta_{jl}) e_{kl} = \lambda\delta_{ij} e_{kk} + 2\mu e_{ij}, \tag{4}$$

where λ and μ are the Lamé coefficients of the solid, while the B^s_{ijkl} all vanish. The corresponding equations of motion are given by

$$\partial_t \mathbf{v} = b^s \mathrm{div}(\tau^s),$$

$$\partial_t \mathbf{u} = \mathbf{v},$$

in $\Omega_s \times [0, T]$, where $b^s := 1/\rho^s$ is the solid buoyancy.

Likewise, the fluid constitutive equations may also be written in the form

$$\tau^f_{ij} = A^f_{ijkl} e(\mathbf{u})_{kl} + B^f_{ijkl} e(\mathbf{v})_{kl}, \tag{5}$$

where assuming viscous dissipation together with small compressibility,[19]

$$A^f_{ijkl} = c^2 \rho^f \delta_{ij} \delta_{kl}, \quad B^f_{ijkl} = 2\eta \delta_{ik} \delta_{jl},$$

with ρ^f and η being the density and dynamic viscosity of the fluid, respectively, and c the speed of sound in the fluid. The corresponding equations of motion read

$$\partial_t \mathbf{v} = b^f \mathrm{div}(\tau^f),$$

$$\partial_t \mathbf{u} = \mathbf{v},$$

in $\Omega_f \times [0, T]$, where $b^f := 1/\rho^f$ is the fluid buoyancy.

In this paper, as we consider a mixture theory approach, we replace Θ by β, the porosity. Hence, by combining the solid and fluid phases, the resulting composite system has the constitutive equation

$$\tau_{ij} = \beta[c^2 \rho^f \delta_{ij} e(\mathbf{u})_{kk} + 2\eta e(\mathbf{v})_{ij}] + (1 - \beta)[\lambda \delta_{ij} e(\mathbf{u})_{kk} + 2\mu e(\mathbf{u})_{ij}].$$

The corresponding equations of motion take the form

$$\partial_t \mathbf{v} = \beta b^f \mathrm{div}(\tau^f) + (1 - \beta) b^s \mathrm{div}(\tau^s), \tag{6a}$$

$$\partial_t \tau = \beta[c^2 \rho^f \mathrm{div}(\mathbf{v}\mathbb{I}) + 2\eta e(\partial_t \mathbf{v})] + (1 - \beta)[\lambda\, \mathrm{div}(\mathbf{v}\mathbb{I}) + 2\mu e(\mathbf{v})], \tag{6b}$$

$$\partial_t \mathbf{u} = \mathbf{v}, \tag{6c}$$

where $\mathbb{I}$ is the identity tensor, and the term $e(\partial_t \mathbf{v})$ appearing in (6b) must be rewritten using the expression given for $\partial_t \mathbf{v}$ in (6a). These are the linearized equations for acoustic propagation through the composite material, which will be used in our numerical experiments. In the next sections, we present in detail the numerical scheme to solve the equations for each phase.

2.1. *Numerical scheme for the solid phase*

Trabecular bone is essentially cortical and we may approximate it for acoustical purposes as being elastic. If it is also isotropic,[a] this leads to the system described by (2) and (4).

[a]It is most likely orthotropic.

Hence, considering the general three-dimensional case in Cartesian coordinates (x, y, z), the stresses become

$$\begin{aligned}
\tau^s_{xx} &= (\lambda + 2\mu)\partial_x u_x + \lambda(\partial_y u_y + \partial_z u_z),\\
\tau^s_{yy} &= (\lambda + 2\mu)\partial_y u_y + \lambda(\partial_x u_x + \partial_z u_z),\\
\tau^s_{zz} &= (\lambda + 2\mu)\partial_z u_z + \lambda(\partial_x u_x + \partial_y u_y),\\
\tau^s_{xy} &= \mu(\partial_x u_y + \partial_y u_x),\\
\tau^s_{xz} &= \mu(\partial_x u_z + \partial_z u_x),\\
\tau^s_{yz} &= \mu(\partial_y u_z + \partial_z u_y),
\end{aligned} \tag{7}$$

and their evolution is governed by

$$\begin{aligned}
\partial_t\tau^s_{xx} &= (\lambda + 2\mu)\partial_x v_x + \lambda(\partial_y v_y + \partial_z v_z),\\
\partial_t\tau^s_{yy} &= (\lambda + 2\mu)\partial_y v_y + \lambda(\partial_x v_x + \partial_z v_z),\\
\partial_t\tau^s_{zz} &= (\lambda + 2\mu)\partial_z v_z + \lambda(\partial_x v_x + \partial_y v_y),\\
\partial_t\tau^s_{xy} &= \mu(\partial_x v_y + \partial_y v_x),\\
\partial_t\tau^s_{xz} &= \mu(\partial_x v_z + \partial_z v_x),\\
\partial_t\tau^s_{yz} &= \mu(\partial_y v_z + \partial_z v_y).
\end{aligned} \tag{8}$$

The equations of motion for the velocity field read

$$\begin{aligned}
\rho^s\partial_t v_x &= \partial_x\tau^s_{xx} + \partial_y\tau^s_{xy} + \partial_z\tau^s_{xz},\\
\rho^s\partial_t v_y &= \partial_x\tau^s_{xy} + \partial_y\tau^s_{yy} + \partial_z\tau^s_{yz},\\
\rho^s\partial_t v_z &= \partial_x\tau^s_{xz} + \partial_y\tau^s_{yz} + \partial_z\tau^s_{zz},
\end{aligned} \tag{9}$$

and are supplemented by the evolution equations for the displacement field,

$$\partial_t u_x = v_x, \quad \partial_t u_y = v_y, \quad \partial_t u_z = v_z. \tag{10}$$

Following Graves,[22] we use a staggered-grid finite difference method to solve the above system of equations. This method is staggered and second-order in both space and time. The computational domain is a regular volume of space that is divided into unit cubic cells. A sketch of a unit cell is shown in Fig. 1. On a standard collocated grid, spurious oscillations in the numerical solution may occur, due to the phenomenon of decoupling, if centered finite differences are employed. The use of a staggered grid, where the various variables are defined at different nodes in the unit cells, overcomes this difficulty while achieving high accuracy with relatively simple finite difference formulas.

The discretized forms of (8) and (9) are given by

$$\tau^{s\,n+1}_{xx\,i,j,k} = \tau^{s\,n}_{xx\,i,j,k} + \Delta t[(\lambda + 2\mu)D_x v_x + \lambda(D_y v_y + D_z v_z)]^{n+\frac{1}{2}}_{i,j,k},$$

$$\tau^{s\,n+1}_{yy\,i,j,k} = \tau^{s\,n}_{yy\,i,j,k} + \Delta t[(\lambda + 2\mu)D_y v_y + \lambda(D_x v_x + D_z v_z)]^{n+\frac{1}{2}}_{i,j,k},$$

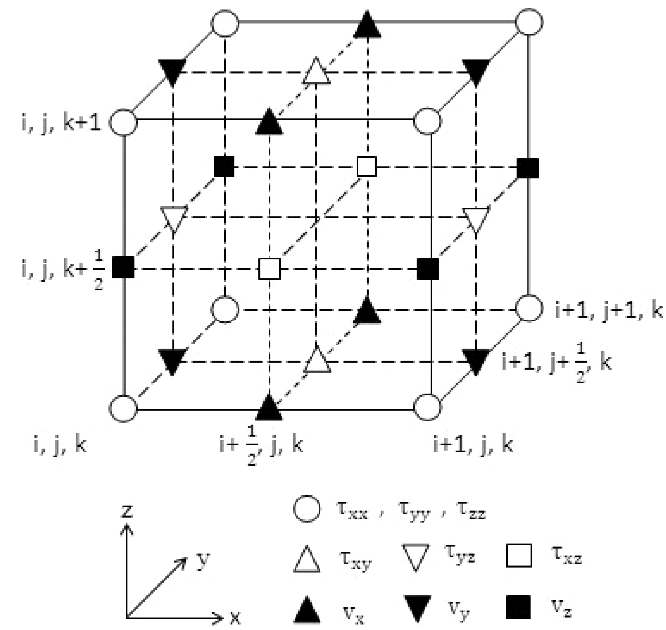

Fig. 1. Sketch of a unit cell in the staggered-grid formulation. The (i, j, k) indices refer to the Cartesian coordinates (x, y, z), respectively.

$$
\begin{aligned}
\tau^{s\,n+1}_{zz\,i,j,k} &= \tau^{s\,n}_{zz\,i,j,k} + \Delta t[(\lambda + 2\mu)D_z v_z + \lambda(D_x v_x + D_y v_y)]^{n+\frac{1}{2}}_{i,j,k},\\
\tau^{s\,n+1}_{xy\,i+\frac{1}{2},j+\frac{1}{2},k} &= \tau^{s\,n}_{xy\,i+\frac{1}{2},j+\frac{1}{2},k} + \Delta t[\mu(D_x v_y + D_y v_x)]^{n+\frac{1}{2}}_{i+\frac{1}{2},j+\frac{1}{2},k},\\
\tau^{s\,n+1}_{xz\,i+\frac{1}{2},j,k+\frac{1}{2}} &= \tau^{s\,n}_{xz\,i+\frac{1}{2},j,k+\frac{1}{2}} + \Delta t[\mu(D_x v_z + D_z v_x)]^{n+\frac{1}{2}}_{i+\frac{1}{2},j,k+\frac{1}{2}},\\
\tau^{s\,n+1}_{yz\,i,j+\frac{1}{2},k+\frac{1}{2}} &= \tau^{s\,n}_{zz\,i,j+\frac{1}{2},k+\frac{1}{2}} + \Delta t[\mu(D_y v_z + D_z v_y)]^{n+\frac{1}{2}}_{i,j+\frac{1}{2},k+\frac{1}{2}},
\end{aligned}
\tag{11}
$$

for the stress components, and

$$
\begin{aligned}
v^{n+\frac{1}{2}}_{x\,i+\frac{1}{2},j,k} &= v^{n-\frac{1}{2}}_{x\,i+\frac{1}{2},j,k} + b^s \Delta t[D_x \tau^s_{xx} + D_y \tau^s_{xy} + D_z \tau^s_{xz}]^n_{i+\frac{1}{2},j,k},\\
v^{n+\frac{1}{2}}_{y\,i,j+\frac{1}{2},k} &= v^{n-\frac{1}{2}}_{y\,i,j+\frac{1}{2},k} + b^s \Delta t[D_x \tau^s_{xy} + D_y \tau^s_{yy} + D_z \tau^s_{yz}]^n_{i,j+\frac{1}{2},k},\\
v^{n+\frac{1}{2}}_{z\,i,j,k+\frac{1}{2}} &= v^{n-\frac{1}{2}}_{z\,i,j,k+\frac{1}{2}} + b^s \Delta t[D_x \tau^s_{xz} + D_y \tau^s_{yz} + D_z \tau^s_{zz}]^n_{i,j,k+\frac{1}{2}},
\end{aligned}
\tag{12}
$$

for the velocity components. In our notation, the subscripts refer to the spatial indices while the superscripts refer to the time index. For example, the expression $v^{n+\frac{1}{2}}_{x\,i+\frac{1}{2},j,k}$ represents the x-component of the velocity at point $x_{i+1/2} = (i + 1/2)\Delta x$, $y_j = j\Delta y$, $z_k = k\Delta z$ and at time $t_{n+1/2} = (n + 1/2)\Delta t$, where Δx, Δy, Δz are the mesh sizes in the three spatial directions (i.e. the dimensions of the unit cell) and Δt is the time step. To avoid overly cumbersome expressions, D_j denotes the difference operator for the discretization of the partial derivative ∂_j in space. The reader is referred to Appendix A for details on these difference operators.

In the present formulation, Eqs. (11) and (12) form a closed system of equations for the stress and velocity fields. An auxiliary computation determines the displacements from the velocities at every time step, assuming their respective components are defined at the same grid points but staggered temporally. Using second-order centered finite differences in time, the discretization of (10) is given by

$$\begin{aligned} u^{n+1}_{x\,i+\frac{1}{2},j,k} &= u^{n}_{x\,i+\frac{1}{2},j,k} + \Delta t\, v^{n+\frac{1}{2}}_{x\,i+\frac{1}{2},j,k}, \\ u^{n+1}_{y\,i,j+\frac{1}{2},k} &= u^{n}_{y\,i,j+\frac{1}{2},k} + \Delta t\, v^{n+\frac{1}{2}}_{y\,i,j+\frac{1}{2},k}, \\ u^{n+1}_{z\,i,j,k+\frac{1}{2}} &= u^{n}_{z\,i,j,k+\frac{1}{2}} + \Delta t\, v^{n+\frac{1}{2}}_{z\,i,j,k+\frac{1}{2}}. \end{aligned} \tag{13}$$

2.2. *Numerical scheme for the fluid phase*

We now turn to the fluid phase. In Cartesian coordinates, the evolution equations for the stress field (5) become

$$\begin{aligned} \partial_t \tau^f_{xx} &= c^2 \rho^f (\partial_x v_x + \partial_y v_y + \partial_z v_z) + 2\eta \partial_x \dot{v}_x, \\ \partial_t \tau^f_{yy} &= c^2 \rho^f (\partial_x v_x + \partial_y v_y + \partial_z v_z) + 2\eta \partial_y \dot{v}_y, \\ \partial_t \tau^f_{zz} &= c^2 \rho^f (\partial_x v_x + \partial_y v_y + \partial_z v_z) + 2\eta \partial_z \dot{v}_x, \\ \partial_t \tau^s_{xy} &= \eta(\partial_x \dot{v}_y + \partial_y \dot{v}_x), \\ \partial_t \tau^s_{xz} &= \eta(\partial_x \dot{v}_z + \partial_z \dot{v}_x), \\ \partial_t \tau^s_{yz} &= \eta(\partial_y \dot{v}_z + \partial_z \dot{v}_y), \end{aligned} \tag{14}$$

where the dot stands for differentiation with respect to time, and the evolution equations for the velocity field are similar to those in the solid phase, i.e.

$$\begin{aligned} \rho^f \partial_t v_x &= \partial_x \tau^f_{xx} + \partial_y \tau^f_{xy} + \partial_z \tau^f_{xz}, \\ \rho^f \partial_t v_y &= \partial_x \tau^f_{xy} + \partial_y \tau^f_{yy} + \partial_z \tau^f_{yz}, \\ \rho^f \partial_t v_z &= \partial_x \tau^f_{xz} + \partial_y \tau^f_{yz} + \partial_z \tau^f_{zz}. \end{aligned} \tag{15}$$

Following the staggered-grid finite difference scheme described previously, the discretization of (14) reads

$$\begin{aligned} \tau^{f\,n+1}_{xx\,i,j,k} &= \tau^{f\,n}_{xx\,i,j,k} + \Delta t[c^2 \rho^f (D_x v_x + D_y v_y + D_z v_z) + 2\eta D_x \dot{v}_x]^{n+\frac{1}{2}}_{i,j,k}, \\ \tau^{f\,n+1}_{yy\,i,j,k} &= \tau^{f\,n}_{yy\,i,j,k} + \Delta t[c^2 \rho^f (D_x v_x + D_y v_y + D_z v_z) + 2\eta D_y \dot{v}_y]^{n+\frac{1}{2}}_{i,j,k}, \end{aligned}$$

$$
\begin{aligned}
\tau^{f\,n+1}_{zz\,i,j,k} &= \tau^{f\,n}_{zz\,i,j,k} + \Delta t[c^2\rho^f(D_x v_x + D_y v_y + D_z v_z) + 2\eta D_z \dot{v}_z]^{n+\frac{1}{2}}_{i,j,k},\\
\tau^{f\,n+1}_{xy\,i+\frac{1}{2},j+\frac{1}{2},k} &= \tau^{f\,n}_{xy\,i+\frac{1}{2},j+\frac{1}{2},k} + \Delta t[\eta(D_x\dot{v}_y + D_y\dot{v}_x)]^{n+\frac{1}{2}}_{i+\frac{1}{2},j+\frac{1}{2},k},\\
\tau^{f\,n+1}_{xz\,i+\frac{1}{2},j,k\frac{1}{2}} &= \tau^{f\,n}_{xz\,i+\frac{1}{2},j,k+\frac{1}{2}} + \Delta t[\eta(D_x\dot{v}_z + D_z\dot{v}_x)]^{n+\frac{1}{2}}_{i+\frac{1}{2},j,k+\frac{1}{2}},\\
\tau^{f\,n+1}_{yz\,i,j+\frac{1}{2},k+\frac{1}{2}} &= \tau^{f\,n}_{yz\,i,j+\frac{1}{2},k+\frac{1}{2}} + \Delta t[\eta(D_y\dot{v}_z + D_z\dot{v}_y)]^{n+\frac{1}{2}}_{i,j+\frac{1}{2},k+\frac{1}{2}},
\end{aligned} \tag{16}
$$

and that for (15) is similar to (12). The acceleration field $\dot{\mathbf{v}} = \partial_t \mathbf{v}$ that appears in (16) is defined at the same nodes as for the velocity field $\mathbf{v}$, and is directly evaluated from (15). Details on the difference operators applied to $\dot{\mathbf{v}}$ can be found in Appendix A. The displacements are again computed by integrating the velocities in time similarly to (13).

Since the time-stepping procedure is explicit, it is thus conditionally stable. A von Neumann stability analysis of the fluid–solid system, estimating an upper bound for the time step as a function of the spatial resolution, is provided in Appendix B.

2.3. *Boundary conditions*

The present stress–velocity formulation combined with the use of a staggered grid is especially suitable for simulating free-surface boundary conditions. The typical physical situation that we have in mind is an *in vitro* experiment with a bone sample immersed in a water tank.[30] We also assume that the boundary is in the solid phase, which is a natural choice for real bones.

Therefore, assuming the domain (i.e. the bone sample) is a rectangular cuboid and considering e.g. the right face of its boundary located at say $i = i_0$, the zero Dirichlet condition on τ_{xx} together with the antisymmetry property of τ_{xy} and τ_{xz}[22] imply

$$\tau_{xx}|_{i=i_0} = 0, \tag{17a}$$

$$\tau_{xy}|_{i=i_0-\frac{1}{2}} = -\tau_{xy}|_{i=i_0+\frac{1}{2}}, \tag{17b}$$

$$\tau_{xz}|_{i=i_0-\frac{1}{2}} = -\tau_{xz}|_{i=i_0+\frac{1}{2}}. \tag{17c}$$

Using (7), condition (17a) yields

$$D_x v_x|_{i=i_0} = -\frac{\lambda}{\lambda + 2\mu}(D_y v_y + D_z v_z)|_{i=i_0}, \tag{18}$$

which is used in (11) to update the boundary values of τ_{yy} and τ_{zz}. Conditions (17b) and (17c), on the other hand, specify values of τ_{xy} and τ_{xz} at "fictitious" nodes $i = i_0 + 1/2$ outside the physical domain, which are used in (12) to compute $D_x\tau_{xy}$ and $D_x\tau_{xz}$ needed to update the boundary values of v_y and v_z. A two-dimensional sketch of the node distribution near the front right corner of the boundary is shown in Fig. 2.

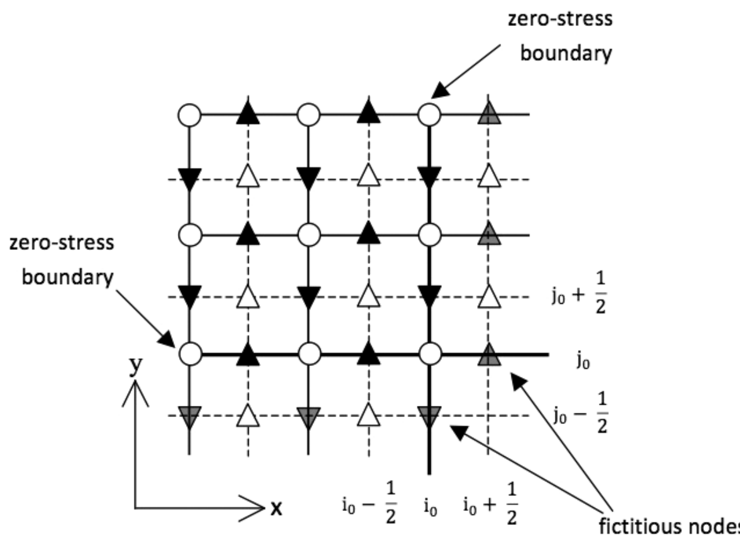

Fig. 2. Top view of the node distribution in the (x, y)-plane near the front right corner of the boundary. The velocities are in black for interior nodes and in gray for fictitious exterior nodes. The boundary is represented by the straight lines $i = i_0$ and $j = j_0$.

Similarly, considering the front face of the boundary located at say $j = j_0$, the zero Dirichlet condition on τ_{yy} together with the antisymmetry property of τ_{yx} and τ_{yz} imply

$$\tau_{yy}|_{j=j_0} = 0, \tag{19a}$$

$$\tau_{yx}|_{j=j_0-\frac{1}{2}} = -\tau_{yx}|_{j=j_0+\frac{1}{2}}, \tag{19b}$$

$$\tau_{yz}|_{j=j_0-\frac{1}{2}} = -\tau_{yz}|_{j=j_0+\frac{1}{2}}, \tag{19c}$$

with (19a) being equivalent to

$$D_y v_y|_{j=j_0} = -\frac{\lambda}{\lambda + 2\mu}(D_x v_x + D_z v_z)|_{j=j_0}.$$

These conditions enable us to update the boundary values of τ_{xx}, τ_{zz}, v_x and v_z, using values of τ_{yx} and τ_{yz} at fictitious exterior nodes $j = j_0 - 1/2$.

3. Numerical Tests

We present numerical tests of the mixture model (6) which is simulated by combining the discretizations for the solid and fluid phases, as described in the previous sections. For convenience, we restrict ourselves to the two-dimensional case where the domain is a rectangle with sides of length L_x and L_y, divided into N_x and N_y unit cells in the x- and y-directions, respectively. The first test assesses the convergence of our numerical scheme in comparison with an exact solution. The second test assesses the dissipative properties of our model and examines their dependence on ultrasonic frequency.

Table 1. Values of physical parameters for cancellous bone.

Parameter	Symbol	Value
Sound speed in fluid	c	$1497\,\mathrm{m\,s^{-1}}$
Pore fluid density	ρ^f	$950\,\mathrm{kg\,m^{-3}}$
Fluid bulk modulus	K^f	2×10^9 Pa
Pore fluid viscosity	η	$1.5\,\mathrm{N\,s\,m^{-2}}$
Frame material density	ρ^s	$1960\,\mathrm{kg\,m^{-3}}$
Solid bulk modulus	K^s	2.04×10^{10} Pa
Solid shear modulus	μ	0.833×10^{10} Pa
Solid Young's modulus	E	2.2×10^{10} Pa
Poisson's ratio	ν	0.32

Typical values for the physical parameters of the model are given in Table 1.[8,30,33] The Lamé coefficient λ is defined by

$$\lambda = K^b - \frac{2}{3}\mu + \frac{(K^s - K^b)^2 - 2\beta K^s(K^s - K^b) + \beta^2(K^s)^2}{D - K^b},$$

where

$$K^b = \frac{E}{3(1-2\nu)}(1-\beta)^{1.46}, \quad D = K^s\left[1 + \beta\left(\frac{K^s}{K^f} - 1\right)\right].$$

All these parameters are chosen to be real and thus our equations are real-valued.

In our numerical simulations, we also find it convenient to nondimensionalize the equations by using a characteristic time scale T in the ultrasonic range, a characteristic length scale L related to the size of the bone sample and a characteristic density which we choose to be ρ^s. Therefore it is understood that values of dimensional quantities, specified without physical units in the following, are dimensionless values relative to these characteristic scales.

3.1. *Comparison with exact solution*

Let us restrict our attention to the solid phase ($\beta = 0$). In the case of one-dimensional wave propagation, Eqs. (8)–(10) with free-surface boundary condition (18) reduce to the wave equation

$$\partial_t^2 u_x = \frac{\lambda + 2\mu}{\rho^s}\partial_x^2 u_x, \tag{20}$$

for the displacement u_x, with reflecting boundary condition $\partial_x u_x = 0$ at both endpoints $x = 0$ and $x = L_x$. The corresponding stress and velocity are determined by

$$\tau_{xx} = (\lambda + 2\mu)\partial_x u_x, \quad v_x = \partial_t u_x.$$

Given initial conditions

$$u_x = f(x), \quad \partial_t u_x = 0,$$

centered at $x = L_x/2$ and considering only the first rebound off the endpoints, Eq. (20) admits the exact d'Alembert solution

$$u_x = \frac{1}{2}[f(x + c^s t) + f(x - c^s t)],$$

$$v_x = \frac{1}{2}c^s[f'(x + c^s t) - f'(x - c^s t)],$$

$$\tau_{xx} = \frac{1}{2}(\lambda + 2\mu)[f'(x + c^s t) + f'(x - c^s t)],$$

if $x - c^s t > 0$, $x + c^s t < L_x$, and

$$u_x = \frac{1}{2}[f(2L_x - x - c^s t) + f(c^s t - x)],$$

$$v_x = -\frac{1}{2}c^s[f'(2L_x - x - c^s t) - f'(c^s t - x)],$$

$$\tau_{xx} = -\frac{1}{2}(\lambda + 2\mu)[f'(2L_x - x - c^s t) + f'(c^s t - x)],$$

otherwise, where

$$c^s = \sqrt{\frac{\lambda + 2\mu}{\rho^s}}.$$

To compare with this exact solution, we perform numerical simulations of (8)–(10) using initial conditions

$$u_x(x, y, 0) = f(x) = 0.01e^{-100(x - L_x/2)^2},$$

$$v_x(x, y, 0) = 0,$$

and

$$\tau_{xx}(x, y, 0) = (\lambda + 2\mu)f'(x) = -(\lambda + 2\mu)(2x - L_x)e^{-100(x - L_x/2)^2},$$

which are invariant in the y-direction. The computational domain is a square with sides $L_x = L_y = 3$.

Figure 3 plots the relative L^∞ and L^2 errors between the exact and numerical solutions at $t = 0.5$, for different values of N_x with a fixed $\Delta t = 5 \times 10^{-4}$. The good agreement (on all three variables u_x, v_x and τ_{xx}) with the -2 slope confirms the second-order accuracy in space of our numerical scheme.

Figures 4–6 show the comparison between exact and numerical profiles of u_x, v_x and τ_{xx} in the cross section $y = L_y/2$ at various values of t. The spatial resolution is $N_x \times N_y = 200 \times 200$ and the time step is $\Delta t = 5 \times 10^{-4}$. This simulation includes the splitting of the initial condition into left- and right-moving components, as well as their propagation to and bouncing off the boundaries of the domain. For all three variables, we see that the shape of the profile, the propagation speed and the reflecting boundary condition, as well as the

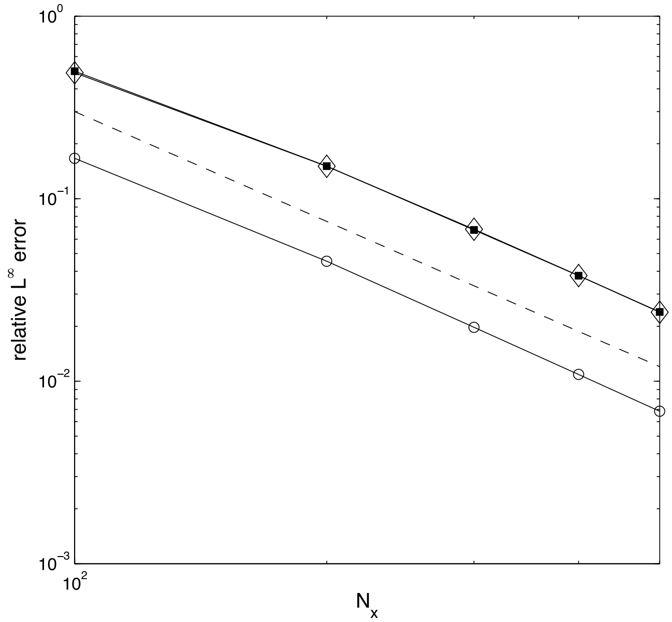

(a)

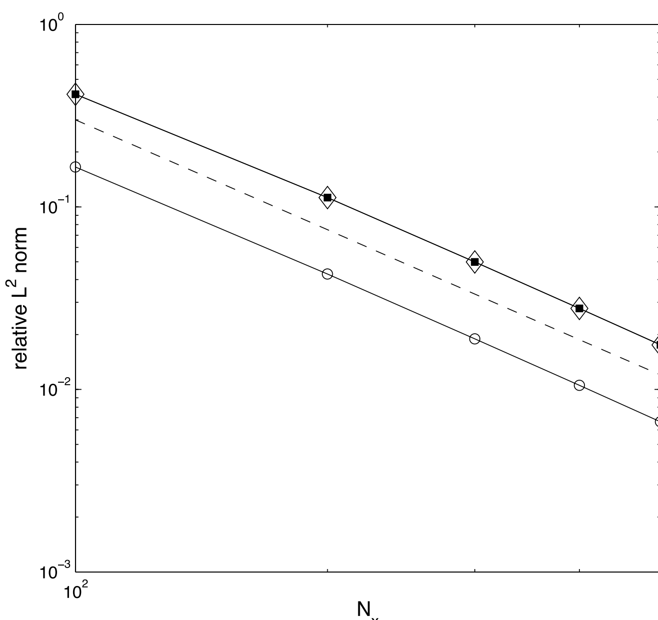

(b)

Fig. 3. Relative (a) L^∞ and (b) L^2 errors versus N_x between the exact and numerical solutions at $t = 0.5$. The displacement u_x is represented in circles, the velocity in diamonds and the stress in squares. For reference, the dashed line represents the curve N_x^{-2} which has a -2 slope in log–log plot.

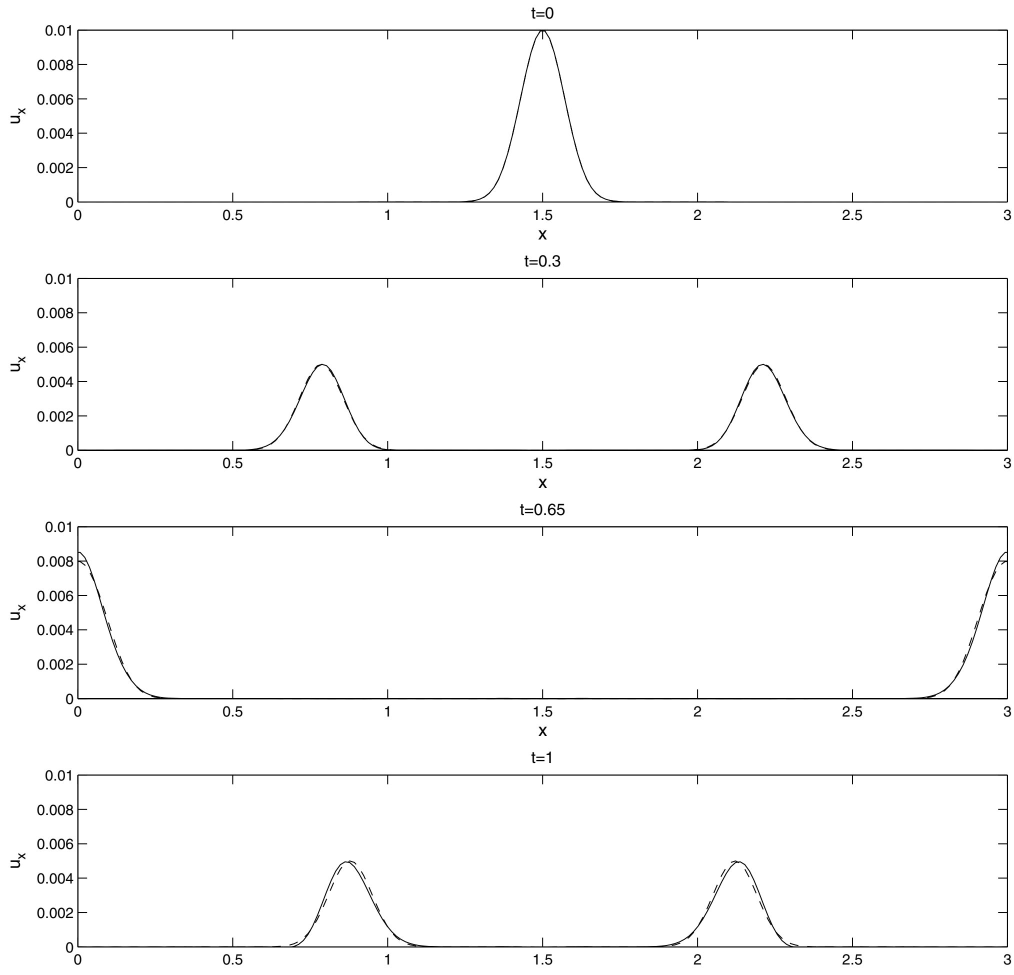

Fig. 4. Profile of displacement u_x in the cross section $y = L_y/2$ at $t = 0$, 0.3, 0.65 and 1. The solid line corresponds to the numerical solution while the dashed line corresponds to the exact solution.

(anti)symmetry of the solution with respect to $x = L_x/2$, are well reproduced numerically. In particular, no visible spurious oscillations nor significant numerical diffusion are observed. Of course, a better agreement can be obtained by increasing the spatial resolution.

3.2. *Ultrasound attenuation*

It is well known that ultrasound propagation through cancellous bone experiences attenuation.[11,33,37] This attenuation is more pronounced at higher frequencies and also increases with bone volume fraction (i.e. bone density). In this section, we check numerically that these features of ultrasound attenuation are reproduced well, at least qualitatively, by our mixture model.

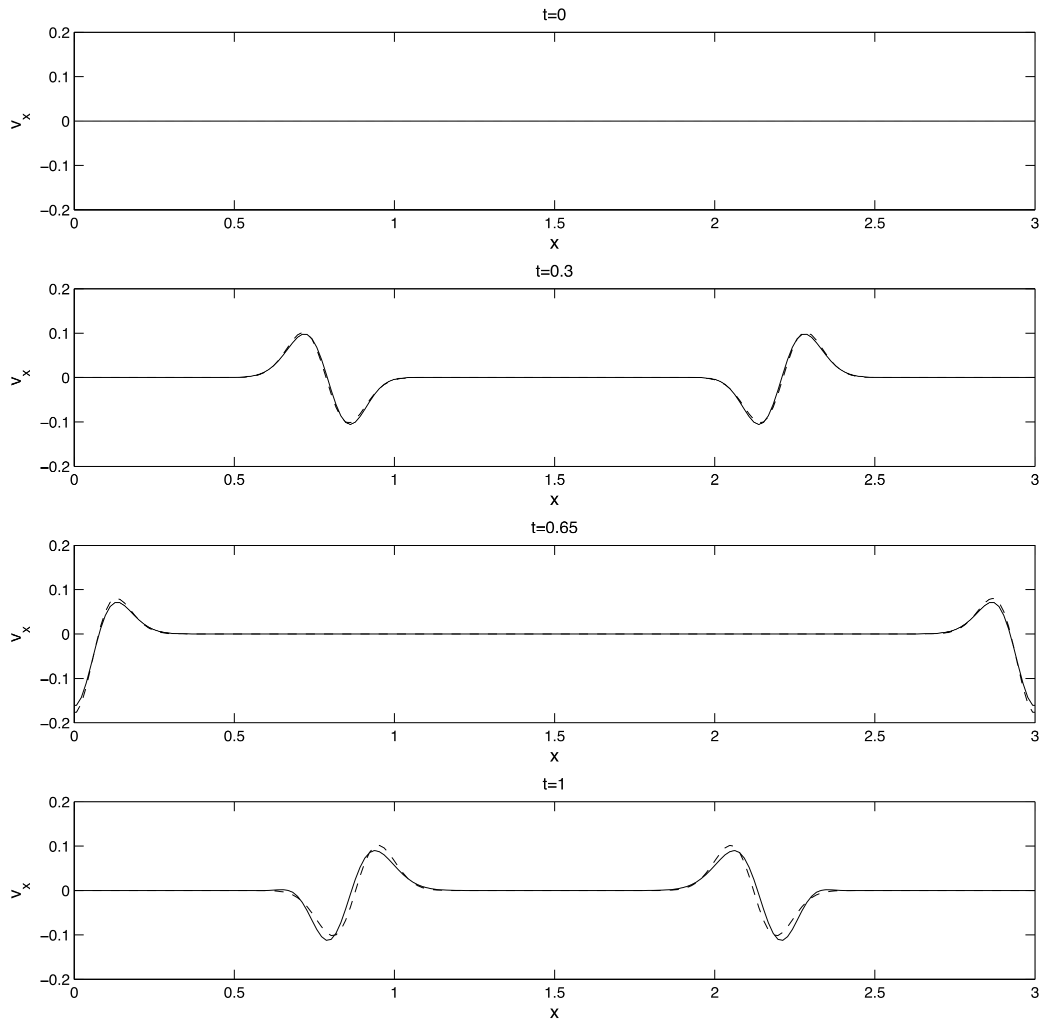

Fig. 5. Profile of velocity v_x in the cross section $y = L_y/2$ at $t = 0$, 0.3, 0.65 and 1. The solid line corresponds to the numerical solution while the dashed line corresponds to the exact solution.

Following Ilic *et al.*,[32,33] the bone sample is assumed to be rectangular, 30 mm long in the x-direction and 50 mm wide in the y-direction. The incoming wave is generated by a localized pressure source, centrally located on the left side of the domain ($x = 0$) and defined by

$$\tau_{xx}(0, y, t) = -P \cos(2\pi f t) e^{-8(y - L_y/2)^2},$$

where f denotes the prescribed temporal frequency, and the mollifier

$$e^{-8(y-L_y/2)^2},$$

is used to avoid discontinuities which may lead to spurious waves propagating in the y-direction. The pressure is applied over a length of about 10 mm on the left side of the bone

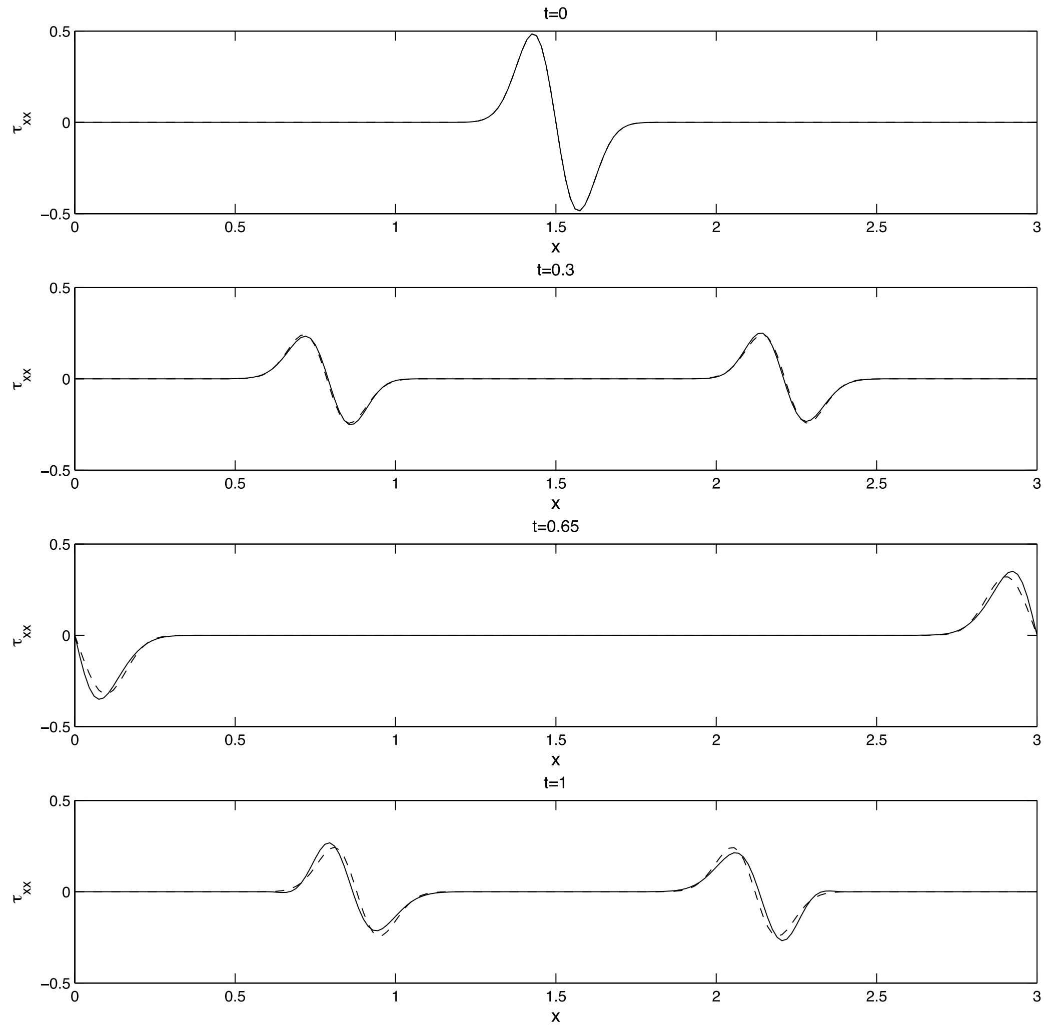

Fig. 6. Profile of stress τ_{xx} in the cross section $y = L_y/2$ at $t = 0$, 0.3, 0.65 and 1. The solid line corresponds to the numerical solution while the dashed line corresponds to the exact solution.

sample. Its amplitude is set to be $P = 8\,\text{kPa}$ and the choice for the porosity is $\beta = 0.82$ so that the average density of our composite medium,

$$\rho = \beta\rho^f + (1 - \beta)\rho^s = 1132\,\text{kg}\,\text{m}^{-3},$$

coincides with that used in Ref. 33. The spatial resolution $N_x \times N_y = 500 \times 500$ and the time step $\Delta t = 5 \times 10^{-4}$ are selected sufficiently fine so they can resolve well the excitation wavelength and period. Since we expect the excitation to be mainly longitudinal, propagating from left to right in the x-direction, we focus our attention on u_x.

Figure 7 shows two-dimensional color plots representing the magnitude of u_x at $t = 1.5$ for viscosity $\eta = 1.5\,\text{N}\,\text{s}\,\text{m}^{-2}$ and frequencies $f = 0.9$, 1.1, 1.4, 1.7 MHz. Cross sections

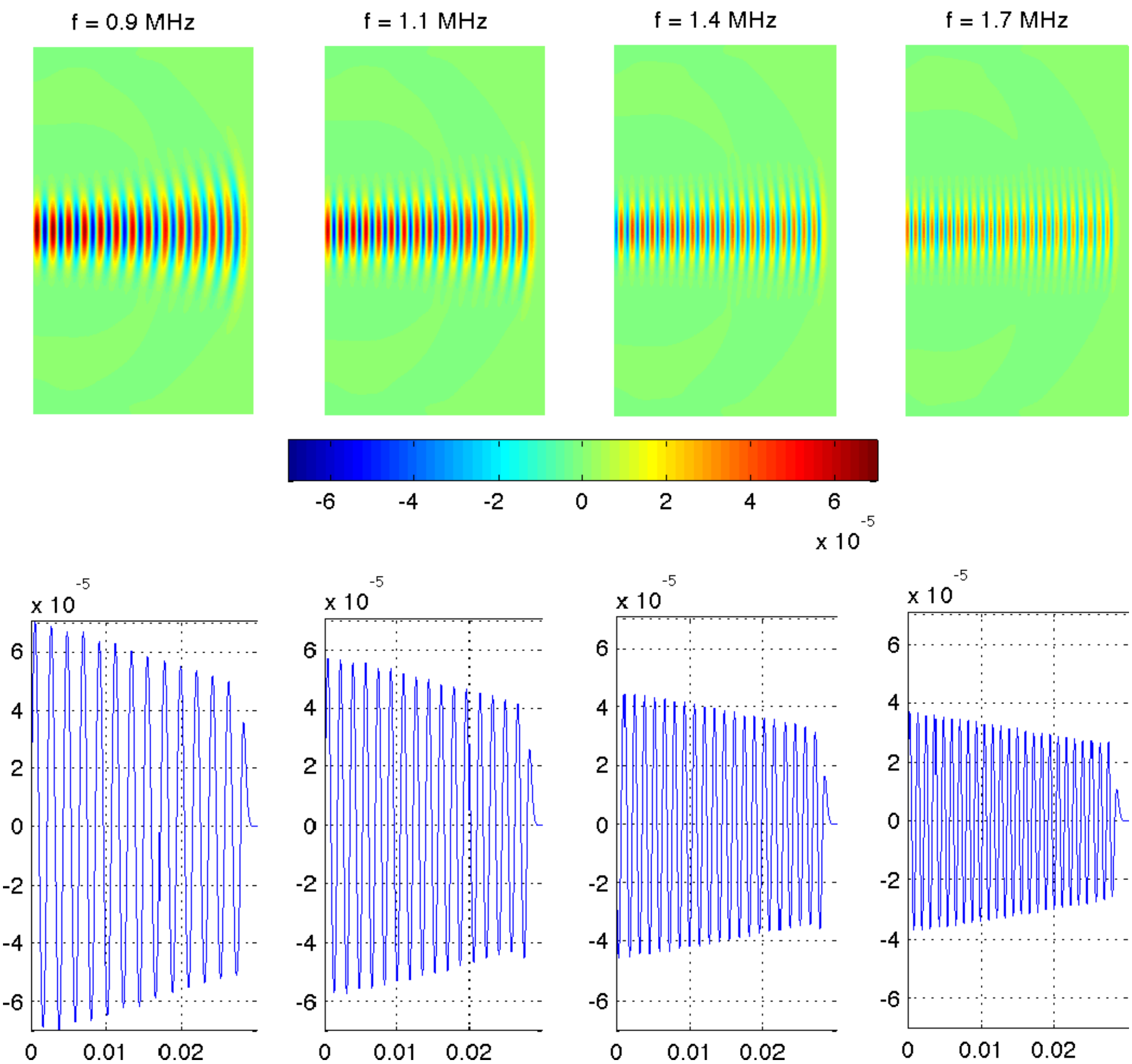

Fig. 7. (Color online) Displacement u_x at $t = 1.5$ for $\beta = 0.82$, $\eta = 1.5\,\mathrm{N\,s\,m^{-2}}$ and $f = 0.9, 1.1, 1.4, 1.7\,\mathrm{MHz}$. Top: two-dimensional color plot. Bottom: cross section at $y = L_y/2$. The values of u_x are magnified by a factor of 10^3.

of u_x at $y = L_y/2$ are also displayed in this figure. As expected, the higher the excitation frequency, the shorter the wavelength. These graphs also clearly reveal that (i) the incoming wave attenuates and diffracts as it travels across the bone sample, and (ii) this attenuation increases with frequency. Wave diffraction, on the other hand, is more apparent at lower frequencies. For clarity, the dimensionless values indicated in Fig. 7 are the computed ones magnified by a factor of 10^3. Therefore, given $T = 10^{-5}\,\mathrm{s}$ and $L = 0.01\,\mathrm{m}$ as used in our nondimensionalization, the actual values of u_x are of order of $10^{-10}\,\mathrm{m}$, which is consistent with those found in Ref. 33. The transverse displacement u_y (not shown here) is typically of an order of magnitude smaller than u_x.

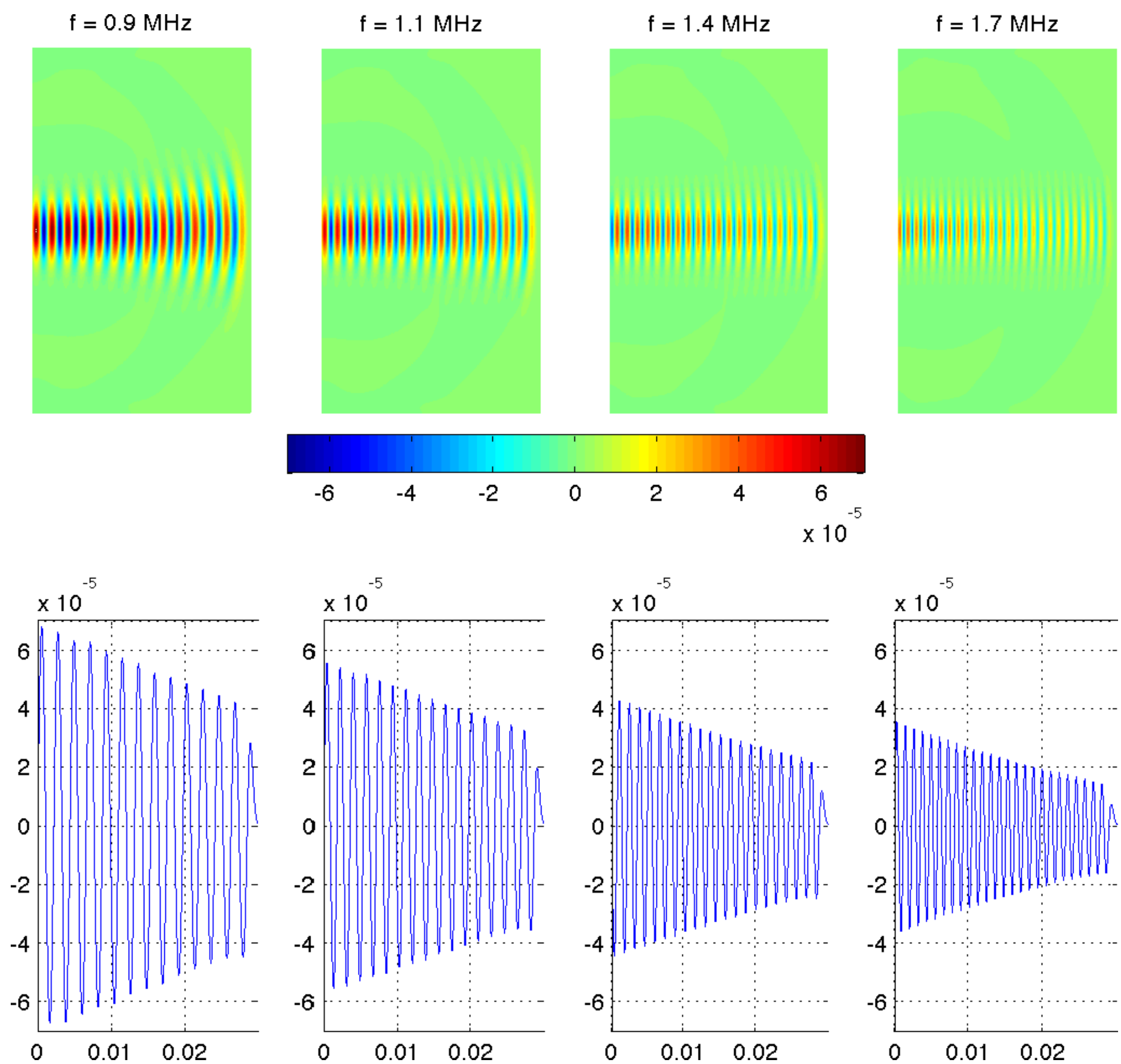

Fig. 8. (Color online) Displacement u_x at $t = 1.5$ for $\beta = 0.82$, $\eta = 5\,\mathrm{N\,s\,m^{-2}}$ and $f = 0.9, 1.1, 1.4, 1.7\,\mathrm{MHz}$. Top: two-dimensional color plot. Bottom: cross section at $y = L_y/2$. The values of u_x are magnified by a factor of 10^3.

Although we observe wave attenuation, we note it is not as significant as that reported in Ref. 33 for similar values of the physical parameters. This may be explained by the fact that we describe the solid part as a purely elastic material without dissipative contributions. Recall the Lamé coefficients λ and μ are assigned real values as listed in Table 1. Therefore, fluid viscosity is the only physical mechanism that controls wave attenuation in our mixture model. Figures 8 and 9 confirm that wave attenuation increases with η. In particular, for $\eta = 8\,\mathrm{N\,s\,m^{-2}}$ (high viscosity) and $f = 1.7\,\mathrm{MHz}$ (high frequency), the incoming wave is so strongly damped that it barely reaches the right side of the bone sample.

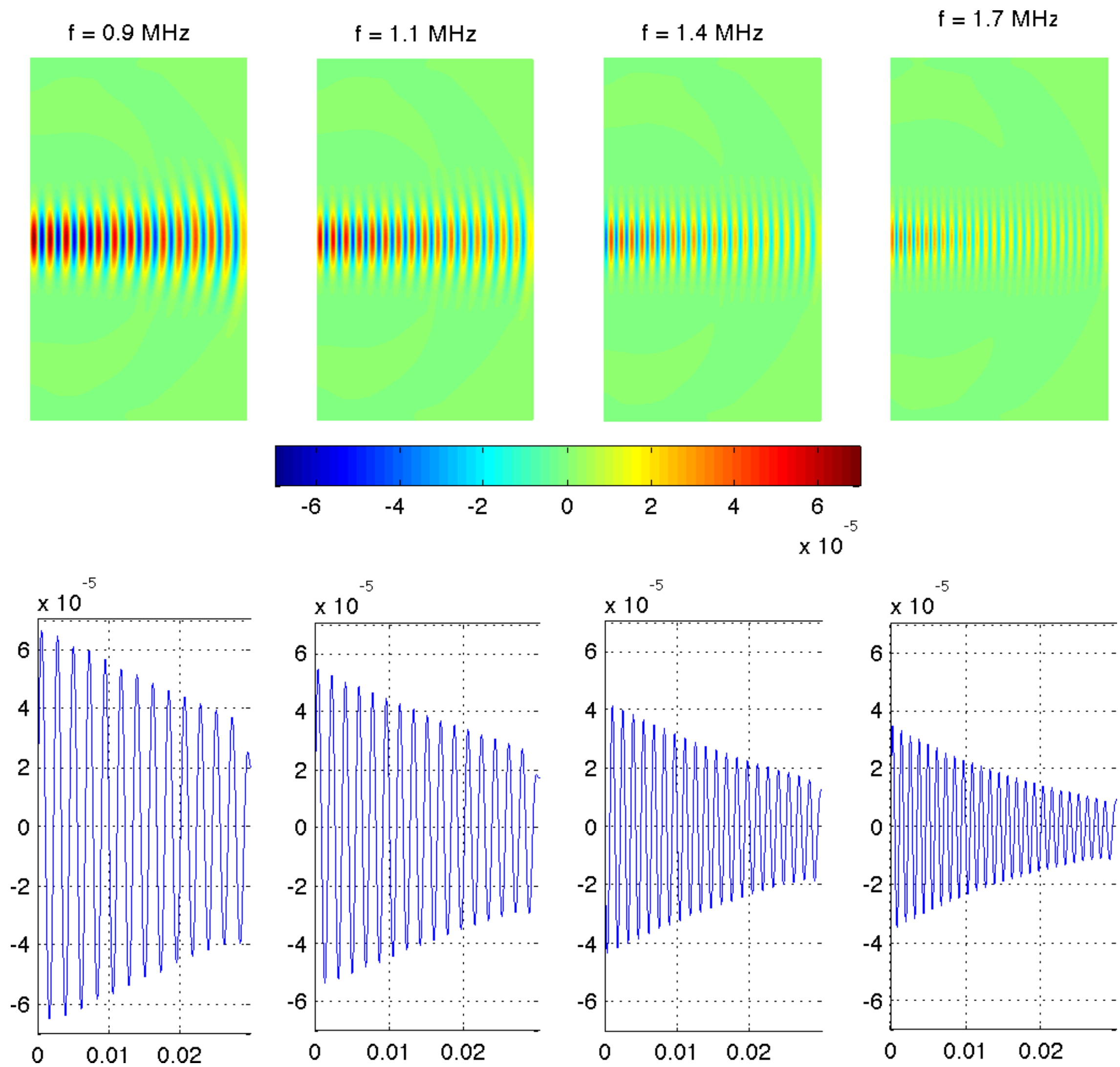

Fig. 9. (Color online) Displacement u_x at $t = 1.5$ for $\beta = 0.82$, $\eta = 8\,\mathrm{N\,s\,m^{-2}}$ and $f = 0.9$, 1.1, 1.4, 1.7 MHz. Top: two-dimensional color plot. Bottom: cross section at $y = L_y/2$. The values of u_x are magnified by a factor of 10^3.

To further quantify this damping, the envelope of the profile of u_x in the cross section $y = L_y/2$ at $t = 1.5$ (before the wave reflects back from the right boundary) is fitted to an exponential function of the form

$$u_x = u_0 e^{-\alpha x},$$

by the method of least squares. The so-obtained coefficient $\alpha > 0$ then yields an estimate for the damping rate through the domain. Figure 10 plots α as a function of f for various values of β and η. We clearly see that the damping rate increases with excitation frequency as well as with bone porosity and viscosity, which is consistent with our previous observations from

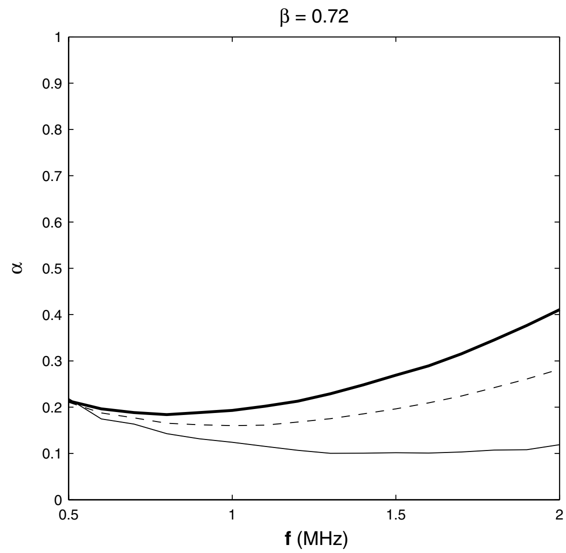

(a) $\beta = 0.72$

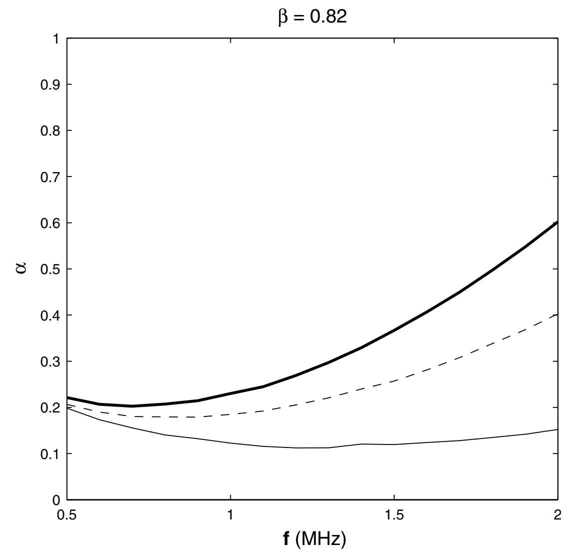

(b) $\beta = 0.82$

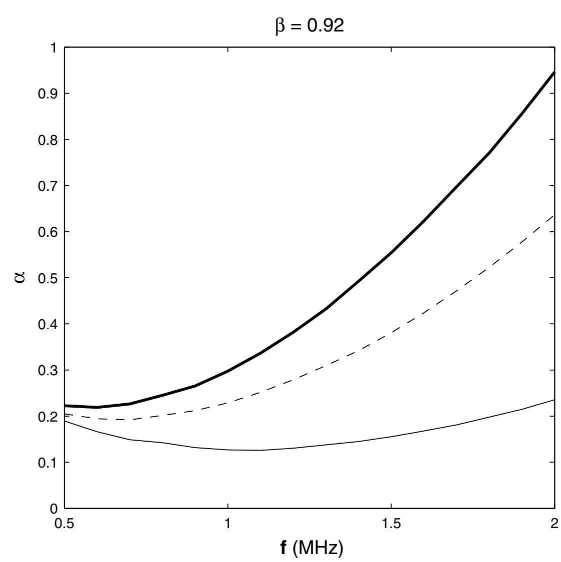

(c) $\beta = 0.92$

Fig. 10. Attenuation rate α as a function of frequency for $\beta = 0.72$, 0.82, 0.92. The thin solid line refers to $\eta = 1.5\,\mathrm{N\,s\,m^{-2}}$, the dashed line to $\eta = 5\,\mathrm{N\,s\,m^{-2}}$ and the thick solid line to $\eta = 8\,\mathrm{N\,s\,m^{-2}}$.

Figs. 7–9. The fact that α increases with f is more apparent for larger values of η. The observed curves suggest that the damping rate grows faster than linearly with frequency, while previous work indicates that it behaves close to linearly.[40] Again, this discrepancy may be attributed to the fact that only the fluid phase is viscous in our mixture model.

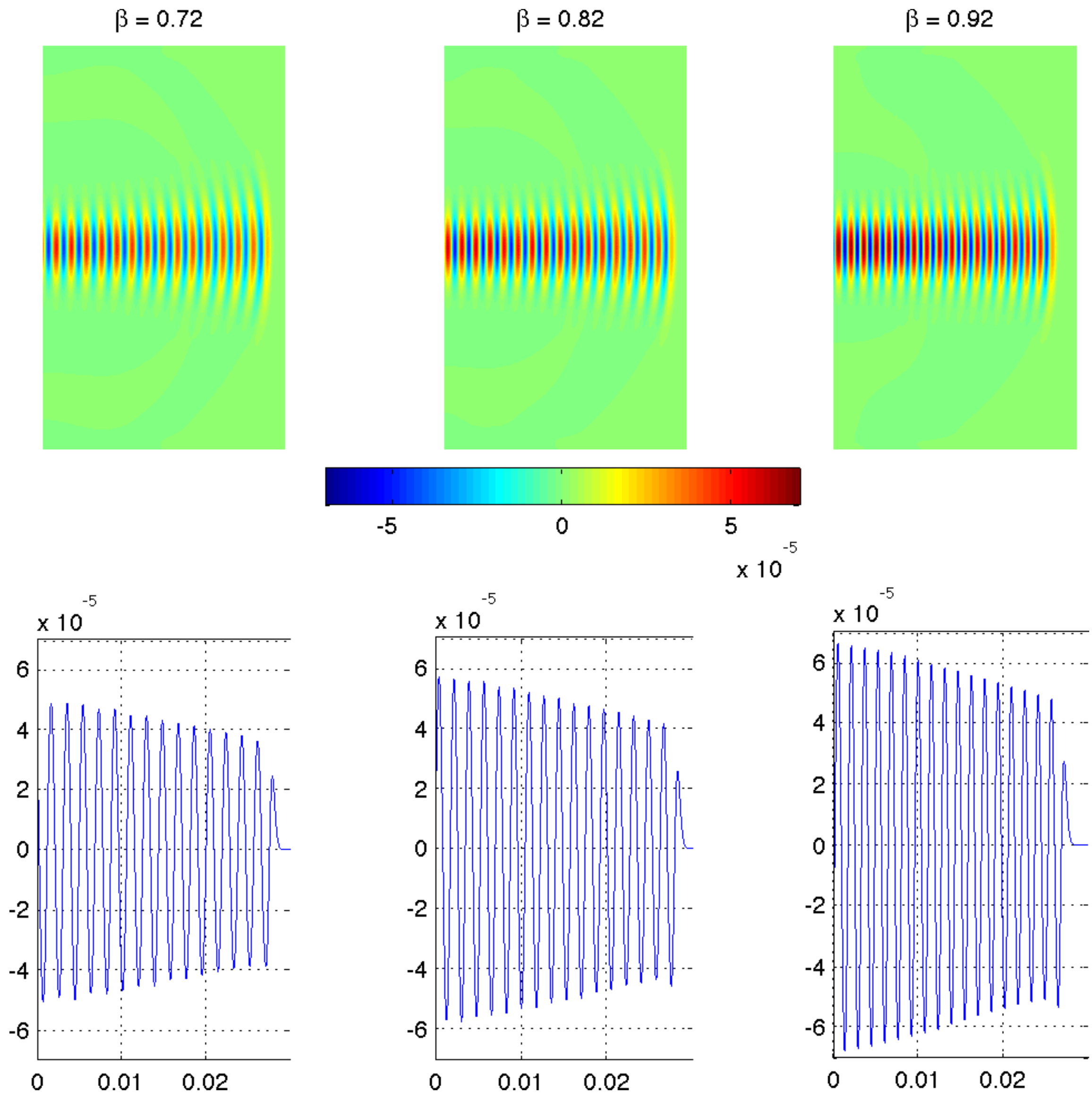

Fig. 11. (Color online) Displacement u_x at $t = 1.5$ for $\eta = 1.5\,\mathrm{N\,s\,m^{-2}}$, $f = 1.1\,\mathrm{MHz}$ and $\beta = 0.72$, 0.82, 0.92. Top: two-dimensional color plot. Bottom: cross section at $y = L_y/2$. The values of u_x are magnified by a factor of 10^3.

Finally, the dependence of wave attenuation on bone porosity is further examined in Fig. 11 which compares the profile of u_x for $\eta = 1.5\,\mathrm{N\,s\,m^{-2}}$, $f = 1.1\,\mathrm{MHz}$ and $\beta = 0.72$, 0.82, 0.92. Note that higher porosity ($\beta = 0.72$, 0.82, 0.92) corresponds to lower average density ($\rho = 1233\,\mathrm{kg\,m^{-3}}$, $1132\,\mathrm{kg\,m^{-3}}$, $1031\,\mathrm{kg\,m^{-3}}$ respectively). Comparing the different amplitudes of u_x, we see that, for higher densities, the composite medium is overall more dissipative and this dissipation is also more uniform spatially, hence the smaller damping

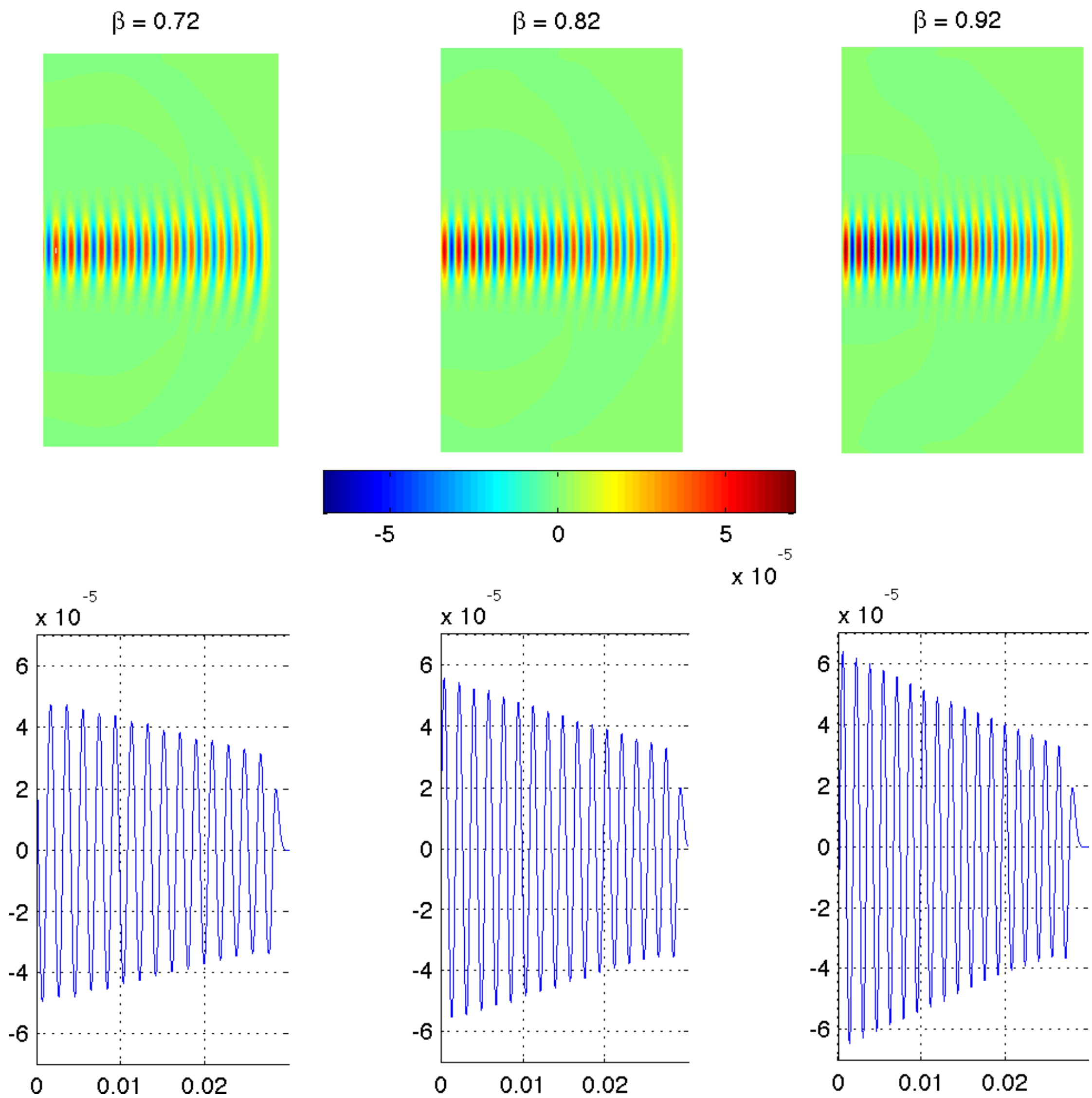

Fig. 12. (Color online) Displacement u_x at $t = 1.5$ for $\eta = 5\,\mathrm{N\,s\,m^{-2}}$, $f = 1.1\,\mathrm{MHz}$ and $\beta = 0.72, 0.82, 0.92$. Top: two-dimensional color plot. Bottom: cross section at $y = L_y/2$. The values of u_x are magnified by a factor of 10^3.

rate as shown in Fig. 10. Similar results are obtained for $\eta = 5$ and $8\,\mathrm{N\,s\,m^{-2}}$ (Figs. 12 and 13). This supports observations made e.g. in Refs. 11, 33 and 37 that wave attenuation tends to increase with bone volume fraction.

4. Conclusion

According to Wear,[63,65] many studies report attenuation to demonstrate an approximately linear dependence on frequency in this range, for instance see Refs. 38–40. However,

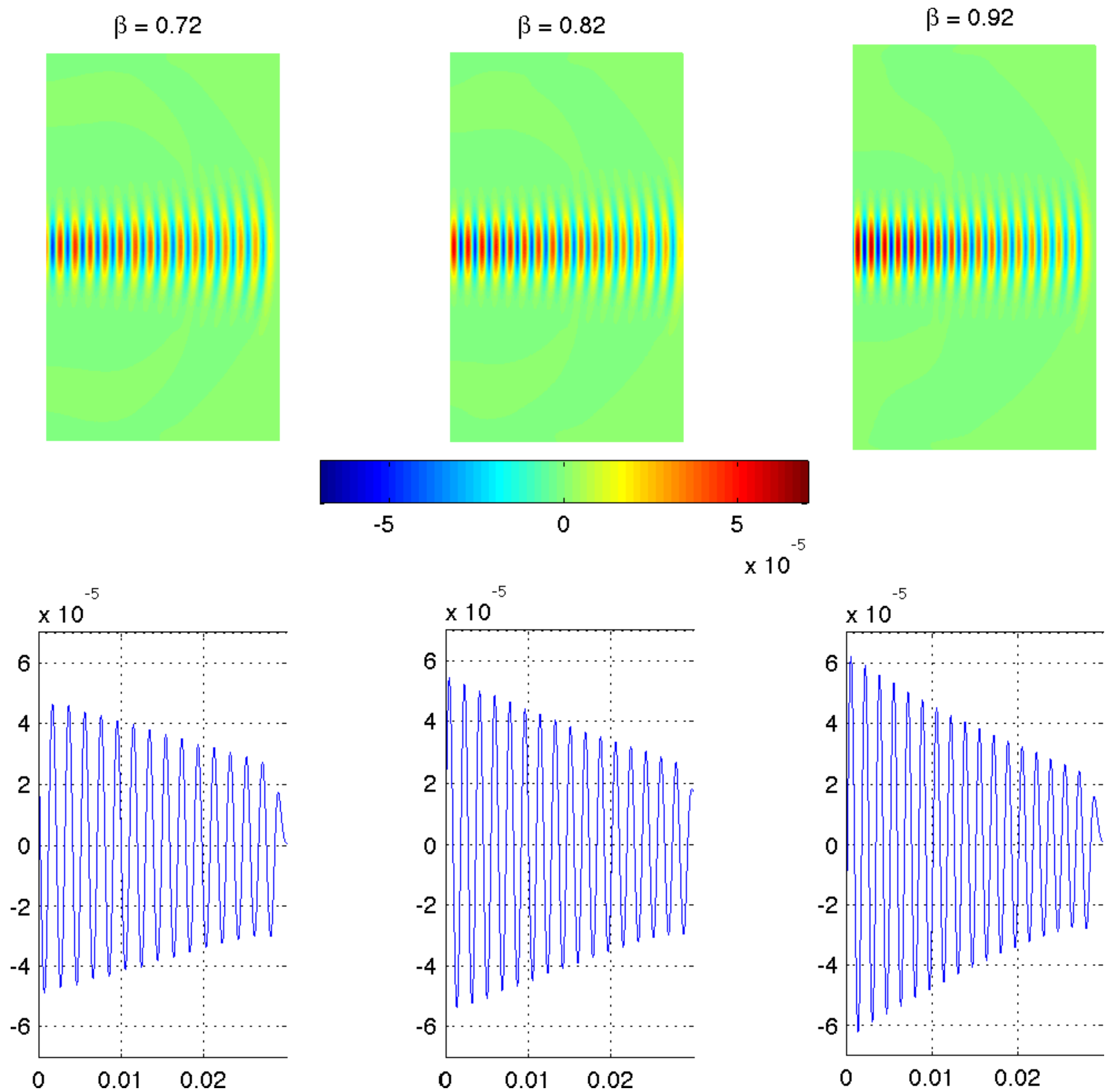

Fig. 13. (Color online) Displacement u_x at $t = 1.5$ for $\eta = 8\,\mathrm{N\,s\,m^{-2}}$, $f = 1.1\,\mathrm{MHz}$ and $\beta = 0.72$, 0.82, 0.92. Top: two-dimensional color plot. Bottom: cross section at $y = L_y/2$. The values of u_x are magnified by a factor of 10^3.

a breakpoint was noticed in the attenuation coefficient versus frequency data near 600 kHz in healthy bone. "Between 200 kHz and 600 kHz, attenuation varied roughly linearly with frequency with a relatively steep slope. Between 600 kHz and 1.0 MHz, the relationship also was approximately linear, but with a noticeably diminished slope". The present model is based on mixture theory. Future work will treat a more exact model where each point of the cancellous bone simulation will be either solid matrix or viscous fluid. Moreover, the solid matrix will have attenuation built into it by using complex parameters which is usually done in bone models. The viscous fluid will be chosen to model a blood–marrow mixture as was done in the recent work.[20]

Acknowledgments

This research was partially sponsored by the National Science Foundation through ARRA-NSF-DMS Grant 0920850 and by the Simons Foundation through Grant 246170. P. Guyenne would like to thank the Institute for Advanced Study (Princeton, NJ) for its hospitality during the academic year 2011–2012.

Appendices

A. Staggered-Grid Finite Difference Operators

We give here the expressions for the second-order finite difference operators D_j that approximate the spatial derivatives ∂_j in the evolution equations for the stress and velocity fields.

The velocity gradient is discretized as follows,

$$D_x v_x|_{i,j,k} = \frac{v_{x\,i+\frac{1}{2},j,k} - v_{x\,i-\frac{1}{2},j,k}}{\Delta x},$$

$$D_y v_y|_{i,j,k} = \frac{v_{y\,i,j+\frac{1}{2},k} - v_{y\,i,j-\frac{1}{2},k}}{\Delta y},$$

$$D_z v_z|_{i,j,k} = \frac{v_{z\,i,j,k+\frac{1}{2}} - v_{z\,i,j,k-\frac{1}{2}}}{\Delta z},$$

which are evaluated at point $x_i = i\Delta x$, $y_j = j\Delta y$ and $z_k = k\Delta z$. The cross-derivatives are approximated by

$$D_x v_y|_{i+\frac{1}{2},j+\frac{1}{2},k} = \frac{v_{y\,i+1,j+\frac{1}{2},k} - v_{y\,i,j+\frac{1}{2},k}}{\Delta x},$$

$$D_y v_x|_{i+\frac{1}{2},j+\frac{1}{2},k} = \frac{v_{x\,i+\frac{1}{2},j+1,k} - v_{x\,i+\frac{1}{2},j,k}}{\Delta y},$$

$$D_x v_z|_{i+\frac{1}{2},j,k+\frac{1}{2}} = \frac{v_{z\,i+1,j,k+\frac{1}{2}} - v_{z\,i,j,k+\frac{1}{2}}}{\Delta x},$$

$$D_z v_x|_{i+\frac{1}{2},j,k+\frac{1}{2}} = \frac{v_{x\,i+\frac{1}{2},j,k+1} - v_{x\,i+\frac{1}{2},j,k}}{\Delta z},$$

$$D_y v_z|_{i,j+\frac{1}{2},k+\frac{1}{2}} = \frac{v_{z\,i,j+1,k+\frac{1}{2}} - v_{z\,i,j,k+\frac{1}{2}}}{\Delta y},$$

$$D_z v_y|_{i,j+\frac{1}{2},k+\frac{1}{2}} = \frac{v_{y\,i,j+\frac{1}{2},k+1} - v_{y\,i,j+\frac{1}{2},k}}{\Delta z}.$$

Note that the superscript denoting the time index is omitted for convenience.

For the stress gradient, its discretized forms are given by

$$D_x\tau_{xx}|_{i+\frac{1}{2},j,k} = \frac{\tau_{xx\,i+1,j,k} - \tau_{xx\,i,j,k}}{\Delta x},$$

$$D_y\tau_{xy}|_{i+\frac{1}{2},j,k} = \frac{\tau_{xy\,i+\frac{1}{2},j+\frac{1}{2},k} - \tau_{xy\,i+\frac{1}{2},j-\frac{1}{2},k}}{\Delta y},$$

$$D_z\tau_{xz}|_{i+\frac{1}{2},j,k} = \frac{\tau_{xz\,i+\frac{1}{2},j,k+\frac{1}{2}} - \tau_{xz\,i+\frac{1}{2},j,k-\frac{1}{2}}}{\Delta z},$$

$$D_x\tau_{xy}|_{i,j+\frac{1}{2},k} = \frac{\tau_{xy\,i+\frac{1}{2},j+\frac{1}{2},k} - \tau_{xy\,i-\frac{1}{2},j+\frac{1}{2},k}}{\Delta x},$$

$$D_y\tau_{yy}|_{i,j+\frac{1}{2},k} = \frac{\tau_{yy\,i,j+1,k} - \tau_{yy\,i,j,k}}{\Delta y},$$

$$D_z\tau_{yz}|_{i,j+\frac{1}{2},k} = \frac{\tau_{yz\,i,j+\frac{1}{2},k+\frac{1}{2}} - \tau_{yz\,i,j+\frac{1}{2},k-\frac{1}{2}}}{\Delta z},$$

$$D_x\tau_{xz}|_{i,j,k+\frac{1}{2}} = \frac{\tau_{xz\,i+\frac{1}{2},j,k+\frac{1}{2}} - \tau_{xz\,i-\frac{1}{2},j,k+\frac{1}{2}}}{\Delta x},$$

$$D_y\tau_{yz}|_{i,j,k+\frac{1}{2}} = \frac{\tau_{yz\,i,j+\frac{1}{2},k+\frac{1}{2}} - \tau_{yz\,i,j-\frac{1}{2},k+\frac{1}{2}}}{\Delta y},$$

$$D_z\tau_{zz}|_{i,j,k+\frac{1}{2}} = \frac{\tau_{zz\,i,j,k+1} - \tau_{zz\,i,j,k}}{\Delta z}.$$

Although we only use second-order approximations in this paper, higher-order formulas can be obtained following the technique of Levander[42] and Yomogida and Etgen.[69]

B. von Neumann Stability Analysis

Through a von Neumann stability analysis, we derive a condition on Δt that ensures stability of the numerical scheme. For convenience, we restrict the analysis to the two-dimensional case as in our numerical simulations. We thus assume a displacement field of the form

$$\mathbf{u}(\mathbf{x}, t) = (\widehat{u}_x, \widehat{u}_y)e^{i(\mathbf{k}\cdot\mathbf{x}-\omega t)}. \tag{B.1}$$

First, let us consider the solid phase. Substituting $\mathbf{v} = \partial_t\mathbf{u}$ and (7) into (9) yields a closed system of equations for the displacement field. The corresponding discretized equations, set up in matrix form, read

$$\begin{bmatrix} (\alpha_s^2 D_{xx} + \beta_s^2 D_{yy}) - D_{tt} & (\alpha_s^2 - \beta_s^2)D_{xy} \\ (\alpha_s^2 - \beta_s^2)D_{xy} & (\alpha_s^2 D_{yy} + \beta_s^2 D_{xx}) - D_{tt} \end{bmatrix} \mathbf{u} = \mathbf{0},$$

where

$$\alpha_s = \sqrt{\frac{\lambda + 2\mu}{\rho^s}}, \quad \beta_s = \sqrt{\frac{\mu}{\rho^s}}.$$

This linear system admits a nontrivial solution if and only if the determinant of the coefficient matrix is zero, which implies

$$\begin{aligned} D_{tt} &= \frac{1}{2}(\alpha_s^2 + \beta_s^2)(D_{xx} + D_{yy}) \\ &\quad \pm \frac{1}{2}(\alpha_s^2 - \beta_s^2)\sqrt{(D_{xx} + D_{yy})^2 - 4(D_{xx}D_{yy} - D_{xy}^2)}. \end{aligned} \tag{B.2}$$

Then substituting (B.1) into (B.2) leads to

$$\begin{aligned} \sin^2 \frac{\omega \Delta t}{2} = \frac{1}{2}\left(\frac{\Delta t}{h}\right)^2 \Bigg\{ &(\alpha_s^2 + \beta_s^2)\left(\sin^2 \frac{k_x h}{2} + \sin^2 \frac{k_y h}{2}\right) \\ &\pm (\alpha_s^2 - \beta_s^2)\left[\left(\sin^2 \frac{k_x h}{2} - \sin^2 \frac{k_y h}{2}\right)^2 \right. \\ &\left. + \left(\cos \frac{(k_x + k_y)h}{2} - \cos \frac{(k_x - k_y)h}{2}\right)^2\right]^{1/2} \Bigg\}, \end{aligned}$$

where $\mathbf{k} = (k_x, k_y)$ and, for simplicity, we assume that $\Delta x = \Delta y = h$. By requiring that the right-hand side be less than or equal to 1, we arrive at the stability condition

$$\Delta t \leq \frac{h}{\sqrt{2}\alpha_s},$$

which is similar to that reported in Ref. 22.

We now turn to the fluid phase. Following the same procedure as before, we obtain the linear system

$$\begin{bmatrix} \alpha_f^2 D_{xx} + \beta_f^2(2D_{xxt} + D_{yyt}) - D_{tt} & \alpha_f^2 D_{xy} + \beta_f^2 D_{xyt} \\ \alpha_f^2 D_{xy} + \beta_f^2 D_{xyt} & \alpha_f^2 + \beta_f^2(2D_{yyt} + D_{xxy}) - D_{tt} \end{bmatrix} \mathbf{u} = \mathbf{0},$$

whose solvability implies

$$\begin{aligned} D_{tt} &= \frac{1}{2}[\alpha_f^2(D_{xx} + D_{yy}) + 3\beta_f^2(D_{xxt} + D_{yyt})] \\ &\quad \pm \frac{1}{2}\sqrt{[\alpha_f^2(D_{xx} - D_{yy})^+ \beta_f^2(D_{xxt} - D_{yyt})]^2 + 4(\alpha_f^2 D_{xy} + \beta_f^2 D_{xyt})^2}, \end{aligned} \tag{B.3}$$

where

$$\alpha_f = c, \quad \sqrt{\beta_f} = \eta/\rho^f.$$

Again, substituting (B.1) into (B.3) leads to

$$\sin^2\frac{\omega\Delta t}{2} = \frac{1}{2}\left(\frac{\Delta t}{h}\right)^2 \Bigg\{\left(\alpha_f^2 + 3\beta_f^2\frac{e^{-i\omega\Delta t}-1}{\Delta t}\right)\left(\sin^2\frac{k_x h}{2} + \sin^2\frac{k_y h}{2}\right)$$
$$\pm\left(\alpha_f^2 + \beta_f^2\frac{e^{-i\omega\Delta t}-1}{\Delta t}\right)\left[\left(\sin^2\frac{k_x h}{2} - \sin^2\frac{k_y h}{2}\right)^2\right.$$
$$\left.+\left(\cos\frac{(k_x+k_y)h}{2} - \cos\frac{(k_x-k_y)h}{2}\right)^2\right]^{\frac{1}{2}}\Bigg\},$$
$$= \frac{1}{2}\left(\frac{\Delta t}{h}\right)^2\left[\alpha_f^2 + 3\beta_f^2\frac{e^{-i\omega\Delta t}-1}{\Delta t}\right.$$
$$\left.\pm\left(\alpha_f^2 + \beta_f^2\frac{e^{-i\omega\Delta t}-1}{\Delta t}\right)\right]\left(\sin^2\frac{k_x h}{2} + \sin^2\frac{k_y h}{2}\right). \tag{B.4}$$

Assuming $\omega\Delta t \ll 1$ so we can Taylor expand

$$\frac{e^{-i\omega\Delta t}-1}{\Delta t} = \frac{1 - i\omega\Delta t + \cdots - 1}{\Delta t} \approx -i\omega,$$

then Eq. (B.4) further simplifies to

$$\sin^2\frac{\omega\Delta t}{2} = \frac{1}{2}\left(\frac{\Delta t}{h}\right)^2\left[\alpha_f^2 - 3i\omega\beta_f^2 \pm (\alpha_f^2 - i\omega\beta_f^2)\right]\left(\sin^2\frac{k_x h}{2} + \sin^2\frac{k_y h}{2}\right).$$

By requiring that the right-hand side be less than or equal to 1, we arrive at the stability condition

$$\Delta t \leq \frac{h}{\sqrt{2}(\alpha_f^4 + 4\omega^2\beta_f^4)^{\frac{1}{4}}}.$$

For the composite model, the time step should thus satisfy

$$\Delta t \leq \min\left\{\frac{h}{\sqrt{2}\alpha_s}, \frac{h}{\sqrt{2}(\alpha_f^4 + 4\omega^2\beta_f^4)^{\frac{1}{4}}}\right\}.$$

A similar analysis would yield stability conditions in higher dimensions.

References

1. R. B. Ashman, S. C. Cowin and J. C. Rice, A continuous wave technique for measurement of the elastic properties of cortical bone, *J. Biomech.* **17** (1984) 349–361.
2. R. B. Ashman, J. D. Corin and C. H. Turner, Elastic properties of cancellous bone: Measurement by ultrasonic technique, *J. Biomech.* **10** (1987) 979–989.

3. R. B. Ashman and J. Y. Rho, Elastic modulus of trabecular bone material, *J. Biomech.* **21** (1988) 177–181.
4. E. Bossy, M. Talmant and P. Laugier, Effect of bone cortical thickness on velocity measurements using ultrasonic axial transmission: A two-dimensional simulation study, *J. Acoust. Soc. Am.* **112** (2002) 297–307.
5. E. Bossy, F. Padilla, F. Peyrin and P. Laugier, Three-dimensional simulation of ultrasound propagation through trabecular bone structures measured by synchrotron microtomography, *Phys. Mech. Biol.* **59** (2005) 5545–5556.
6. J. L. Buchanan and R. P. Gilbert, Measuring osteoporosis using ultrasound, in *Advances in Scattering and Biomedical Engineering*, eds. D. I. Fotiadis and C. V. Massalas (World Scientific, 2004), pp. 484–494.
7. J. L. Buchanan, R. P. Gilbert and K. Khashanah, Determination of the parameters of cancellous bone using low frequency acoustic measurements, *J. Comput. Acoust.* **12** (2004) 99–126.
8. J. Buchanan and R. P. Gilbert, Determination of the parameters of cancellous bone using high frequency acoustic measurements, *Math. Comput. Model.* **45** (2007) 281–308.
9. J. Buchanan and R. P. Gilbert, Determination of the parameters of cancellous bone using high frequency acoustic measurements II: Inverse problems, *J. Comput. Acoust.* **15** (2007) 199–220.
10. J. L. Buchanan, R. P. Gilbert, A. Wirgin and Y. Xu, Transient reflection and transmission of ultrasonic waves in cancellous bones, *Math. Comput. Model.* **142** (2003) 561–573.
11. S. Chaffai, F. Padilla, G. Berger and P. Laugier, In vitro measurement of the frequency dependent attenuation in cancellous bone between 0.2 and 2 MHz, *J. Acoust. Soc. Am.* **108** (2000) 1281–1289.
12. S. Chaffai, V. Roberjot, F. Peyrin, G. Berger and P. Laugier, Frequency dependence of ultrasonic backscattering in cancellous bone: Autocorrelation model and experimental results, *J. Acoust. Soc. Am.* **108** (2000) 2403–2411.
13. S. Chaffai, F. Peyrin, S. Nuzzo, R. Porcher, R. Berger and P. Laugier, Ultrasonic characterization of human cancellous bone using transmission and backscatter measurements: Relationships to density and microstructure, *Bone* **30** (2002) 229–237.
14. Z. E. A. Fellah, Y. Chapelon, S. Berger, W. Lauriks and C. Depollier, Ultrasonic wave propagation in human cancellous bone: Application of Biot theory, *J. Acoust. Soc. Am.* **116** (2004) 61–73.
15. L DeRyck, Z. Fellah, R. Gilbert, J.-P. Groby, E. Ogam, N. Sebaa, J.-Y. Chapelon, C. Depollier, Th. Scotti, A. Wirgin and Y. Xu, Recovery of the mechanical parameters of long bones from their vibroacoustic impulse response, *SAPEM* (2005) 1–13.
16. P. Droin, G. Berger and P. Laugier, Velocity dispersion of acoustic waves in cancellous bone, *IEEE Trans. Ultrason., Ferroelectr., Freq. Control* **45** (1998) 581–592.
17. P. Droin, P. Laugier and G. Berger, Ultrasonic attenuation and dispersion of cancellous bone in the frequency range 200 KHz-600 KHz, *Acoustical Imaging*, Vol. 23 (Plenum Press, New York, 1997), pp. 157–162.
18. F. J. Fry and J. E. Barger, Acoustical properties of the human skull, *J. Acoust. Soc. Am.* **63** (1978) 1576–1590.
19. F. J. H. Gijsen, E. Allanic, F. N. van de Vosse and J. D. Janssen, The influence of the non-Newtonian properties of blood on the flow in large arteries: In steady flow in 90^o curved tube, *J. Biomech.* **32** (1999) 705–713.
20. R. P. Gilbert, P. Guyenne and M. Yvonne Ou, A quantitative ultrasound model of the bone with blood as the interstitial fluid, *Math. Comput. Model.* **55** (2011) 2029–2039.
21. C. C. Glüer, Quantitative ultrasound techniques for the assessment of of osteoporosis: Expert agreement on current state, *J. Bone Miner. Res.* **12** (1997) 1280–1288.

22. R. W. Graves, Simulating seismic wave propagation in 3D elastic media using staggered-grid finite differences, *Bull. Seism. Soc. Am.* **86** (1996) 1091–1106.
23. J.-P. Groby, E. Ogam, A. Wirgin, Z. E. A. Fellah, W. Lauriks, J.-Y. Chapelon, C. Depollier, L. DeRyck, N. Sebaa, R. P. Gilbert and Y. Xu, Two-dimensional mode excitation in a porous slab saturated with air in the high frequency approximation, *SAPEM* (2005) 53–68.
24. T. J. Haire and C. M. Langton, Biot theory: A review of its application to ultrasound propagation through cancellous bone, *Bone* **24** (1999) 291–295.
25. D. M. Hegedus and S. C. Cowin, Bone remodeling- II: Small-strain adaptive elasticity, *J. Elasticity* **6** (1976) 337–352.
26. T. Hildebrand and P. Rüegsegger, A new method for the model independent assessment of thickness in three-dimensional images, *J. Microsc.* **185** (1997) 67–75.
27. T. Hildebrand and P. Rüegsegger, Quantification of bone architecture with structure model index, *Comput. Meth. Biomech. Biomed. Eng.* **1** (1997) 5–23.
28. M. C. Hobatho, J. Y. Rho and R. B. Ashman, Atlas of mechanical properties of human cortical and cancellous bone, in *In Vivo Assessment of Bone Quality by Vibration and Wave Propagation Techniques*, *Pt. II*, eds. G. Van der Perre, G. Lowet. and A. Borgwardt-Christensen (Leuven, 1990), pp. 7–38.
29. B. K. Hofmeister, S. A. Whitten and J. Y. Rao, Low megahertz ultrasonic properties of bovine cancellous bone, *Bone* **26** (2000) 635–642.
30. A. Hosokawa and T. Otani, Ultrasonic wave propagation in bovine cancellous bone, *J. Acoust. Soc. Am.* **101** (1997) 558–562.
31. R. Hodgskinson, C. F. Njeh, J. D. Curey and C. M. Langton, The ability of ultrasound velocity to predict the stiffness of cancellous bone in vitro, *Bone* **21** (1997) 183–190.
32. S. Ilic, K. Hackl and R. P. Gilbert, Application of the multiscale FEM to the modeling of the cancellous bone, *Biomech. Model. Mechanobiol.* **9** (2010) 537–551.
33. S. Ilic, K. Hackl and R. P. Gilbert, Application of a biphasic representative volume element to the simulation of wave propagation through cancellous bone, *J. Comput. Acoust.* **19** (2011) 111–138.
34. C. R. Jacobs, The mechanobiology of cancellous bone structure adaption, *J. Rehab. Res. Devel.* **37** (2000).
35. T. Kundu, *Ultrasonic Nondestructive Evaluation* (CRC Press, Boca Raton, 2004).
36. R. S. Lakes, H. S. Yoon and J. L. Katz, Slow compressional wave propagation in wet human cortical bone, *Science* **220** (1992) 513–515.
37. R. S. Lakes, H. S. Yoon and J. L. Katz, Ultrasonic wave propagation and attenuation in wet bone, *J. Biomed. Eng.* **8** (1986) 143–148.
38. C. M. Langton, S. B. Palmer and R. W. Porter, The measurement of broadband ultrasonic attenuation in cancellous bone, *Eng. Medicine* **13** (1984) 89–91.
39. C. M. Langton, C. F. Njeh, R. Hodgskinson and J. D. Curey, Prediction of mechanical properties of human cancellous by broadbeam ultrasonic attenuation, *Bone* **18** (1996) 495–503.
40. C. M. Langton and C. F. Njeh, *The Physical Measurement of Bone* (IOP, Bristol, 2004).
41. W. Lauriks, J. Thoen, I. Van Ashbroek, G. Lowt and G. Vanderperre, Propagation of ultrasonic pulses through trabecular bone, *J. Phys. Colloq. (Paris)* **4** (1994) 1255–1258.
42. A. R. Levander, Fourth-order finite difference P-SV seismograms, *Geophysics* **53** (1988) 1425–1436.
43. F. Luppé, J.-M. Conoir and H. Franklin, Scattering by a fluid cylinder in a porous medium: Application to trabecular bone, *J. Acoust. Soc. Am.* **111** (2002) 2573–2582.
44. F. Luppé, J.-M. Conoir and H. Franklin, Multiple scattering in trabecular bone: Influences of the marrow viscosity on the effective properties, *J. Acoust. Soc. Am.* **113** (2003) 2889– 2892.

45. F. Luppé, J-M. Conoir and H. Franklin, N-shell cluster in water: Multiple scattering and splitting of resonances, *J. Acoust. Soc. Am.* **115** (2004) 1460–1467.
46. R. B. Martin, Porosity and specific surface of bone, *Crit. Rev. Biomed. Eng.* **10** (1984) 97–222.
47. W. Maurel, Y. Wu, N. M. Thalmann and D. Thalmann, *Biomechanical Models for soft Tissue Simulation* (Springer, Berlin, 1998).
48. T. J. McKelvie and S. B. Palmer, The interaction of ultrasound with cancellous bone, *Phys. Med. Biol.* **36** (1991)1331–1340.
49. C. F. Njeh, D. Hans, T. Fuerst, C. C. Gluer and H. K. Genant, *Quantitative Ultrasound. Assessment of Osteoporosis and Bone Status* (Martin Duniz, London 1999).
50. P. H. F. Nicholson and M. L. Bouxsein, Bone marrow influences quntitative ultrasound measurements in human cancellous bone, *Ultrasound Med. Biol.* **28** (2002) 369–375.
51. E. Ogam, Caractéisation ultrasonore et vibroacoustique de la santé mécanique des os humains, PhD thesis, Université de Provence-Aix Marseille I, Marseille, France (2007) (in French).
52. E. Ogam, A. Wirgin, Z. E. A Fellah, J.-P. Groby, W. Lauriks, J.-Y. Chapelon, C. Depollier, L. DeRyck, N. Sebaa, R. P. Gilbert and Y. Xu, Recovery of the mechanical parameters of long bones from their vibroacoustic impulse response, *SAPEM* (2005) 1–8.
53. E. Ogam, C. Masson, S. Erard, A. Wirgin, Z. E. A Fellah, J.-P. Groby and Y. Xu, On the vibratory response of a human tibia: Comparison of 1D Timoshenko model, 3D fEM and experiment, in *Proc. SFA2006*, Paris (2006).
54. E. Ogam and A. Wirgin, Recovery of the ARMA model parameters from the vibration response of a finite length elastic cylinder using neural networks, in *Proc. ISMA2004*, eds. P. Sas and M. De Munck, Leuven (2004), pp. 2437–2446.
55. F. Padilla, F. Peyrin and P. Laugier, Prediction of backscatter coefficient in trabecular bones using a numerical model of three-dimensional microstructure, *J. Acoust. Soc. Am.* **113** (2003) 1122–1129.
56. C. Picart, J.-M. Piau, H. Galliard and P. Carpentier, Human blood shear yield stress and its hematocrit dependence, *J. Rheol.* **42** (1998) 1–12.
57. J.-Y. Rho, An ultrasonic method for measuring the elastic properties of human tibial cortical and cancellous bone, *Ultrasonics* **34** (1996) 777–783.
58. D. S. Sankara and K. Hemalathab, Non-Newtonian fluid flow model for blood flow through a catheterized artery steady flow, *Appl. Math. Model.* **31** (2007) 1847–1864.
59. T. H. Smit, J. M. Huyghe and S. C. Cowin, Estimation of poroelastic parameters of cortical bone, *J. Biomech.* **35** (2002) 829–835.
60. R. Srelitzki and J. A. Evans, On the measurement of the velocity of ultrasound in the calcis using short pulses, *Eur. J. Ultrasound* **4** (1996) 205–213.
61. G. B. Thurston, Viscoelasticity of human blood, *Biophys. J.* **12** (1972) 1205–1217.
62. L. Wang, S. P. Fritton, S. C. Cowin and S. Weinbaum, Fluid pressure relaxation depends upon osteonal microstructure: Modeling an oscillatory bending experiment, *J. Biomech.* **32** (1999) 663–672.
63. K. A. Wear, Ultrasonic attenuation in human calcaneus from 0.2 to 1.7 MHz, *IEEE Trans. Ultrason., Ferroelectr., Frequ. Control* **48** (2001) 602–608.
64. K. A. Wear, Frequency dependence of ultrasonic backscatter from human trabecular bone: Theory and experiment, *J. Acoust. Soc. Am.* **106** (1999) 3659–3664.
65. K. A. Wear, Fundamental precision limitations for measurements of frequency dependence of backscatter: Applications in tissue-mimicking phantoms and trabecular bone, *J. Acoust. Soc. Am.* **110** (2001) 3275–3282.
66. J. L. Williams, Ultrasonic wave propagation in cancellous and cortical bone: Prediction of some experimental results by Biot's theory, *J. Acoust. Soc. Am.* **91** (1992) 1106–1112.

67. K. L. Williams, D. R. Jackson, E. I. Thorsos, D. Tang and S. G. Schock, Comparison of sound speed and attenuation measured in a sandy sediment to predictions based on the Biot's theory of porous media, *IEEE J. Oceanic Eng.* **27** (2002) 413–428.
68. Y. Xu, Transmission of ultrasonic wave in cancellous bone and evaluation of osteoporosis, in *Acoustics*, *Mechanics*, *and the Related Topics of Mathematical Analysis*, ed. A. Wirgin (World Scientific Publishing, 2003), pp. 265–271.
69. K. Yomogida and J. T. Etgen, 3-D wave propagation in the Los Angeles Basin for the Whittier-Narrows earthquake, *Bull. Seism. Soc. Am.* **83** (1993) 1325–1344.